J Digit Imaging (2015) 28:99–115
DOI 10.1007/s10278-014-9718-8

Texture Feature Analysis for Computer-Aided Diagnosis on Pulmonary Nodules

Fangfang Han · Huafeng Wang · Guopeng Zhang ·
Hao Han · Bowen Song · Lihong Li · William Moore ·
Hongbing Lu · Hong Zhao · Zhengrong Liang

Abstract Differentiation of malignant and benign pulmonary nodules is of paramount clinical importance. Texture features of pulmonary nodules in CT images reflect a powerful character of the malignancy in addition to the geometry-related measures. This study first compared three well-known types of two-dimensional (2D) texture features (Haralick, Gabor, and local binary patterns or local binary pattern features) on CADx of lung nodules using the largest public database founded by Lung Image Database Consortium and Image Database Resource Initiative and then investigated extension from 2D to three-dimensional (3D) space. Quantitative comparison measures were made by the well-established support vector machine (SVM) classifier, the area under the receiver operating characteristic curves (AUC) and the *p* values from hypothesis *t* tests. While the three feature types showed about 90 % differentiation rate, the Haralick features achieved the highest AUC value of 92.70 % at an adequate image slice thickness, where a thinner or thicker thickness will deteriorate the performance due to excessive image noise or loss of axial details. Gain was observed when calculating 2D features on all image slices as compared to the single largest slice. The 3D extension revealed potential gain when an optimal number of directions can be found. All the observations from this systematic investigation study on the three feature types can lead to the conclusions that the Haralick feature type is a better choice, the use of the full 3D data is beneficial, and an adequate tradeoff between image thickness and noise is desired for an optimal CADx performance. These conclusions provide a guideline for further research on lung nodule differentiation using CT imaging.

Keywords Lung CADx · Lung nodule analysis · Haralick features · Gabor features · LBP features

Introduction

Lung cancer is the worldwide leading cause of cancer-related deaths, more than the combination of breast, colon, and prostate cancers [1, 2]. In the past decades, because of the widely use of computer tomography (CT) for lung cancer screening [3], a large and increasing number of pulmonary nodules have been detected each year. The ultimate goal of evaluating the detected nodules is to differentiate the malignant from the benign ones. The task of evaluating a large number of detected nodules by the experts or radiologists can be very burdensome. Therefore, computer-aided diagnosis (CADx) is expected to play an important role in the evaluating task, where the

---

F. Han · H. Wang · H. Han · B. Song · W. Moore · Z. Liang
Department of Radiology, State University of New York, Stony Brook, NY 11794, USA

F. Han · H. Zhao
Northeastern University, Shenyang, Liaoning 110819, China

G. Zhang · H. Lu
Department of Biomedical Engineering, Fourth Military Medical University, Xi'an, Shaanxi 710032, China

B. Song
Department of Applied Mathematics and Statistics, State University of New York, Stony Brook, NY 11794, USA

L. Li
Department of Engineering Science and Physics, City University of New York/CSI, Staten Island, NY 10314, USA

Z. Liang (✉)
State University of New York, 4th Floor, Room 120/HSC, Stony Brook, NY 11794-8460, USA
e-mail: jerome.liang@sunysb.edu

H. Zhao (✉)
Neusoft Company, Room 308, Shenyang, Liaoning 110179, China
e-mail: zhaoh@neusoft.com

extraction of features from detected nodules and the classification of the features are the basic research interests.

Many features have been proposed and investigated for the differentiation task, and the features can be divided into two categories according to their achieving paths, namely, clinical and image features. Clinical features were obtained according to the patient records, such as age, gender, history of cancer, history of smoking, location of cancer, etc. [4–6]. A sophisticated study [7] further presented a comprehensive formula of clinical features to evaluate the suspicious on the malignancy. While these clinical features helped the differentiation to some degrees, the outcome was still not satisfactory. Attribute to medical imaging techniques, such as CT, a large number of image features from pulmonary nodules have been extracted, such as size (diameter or volume), shape, morphology, and texture [8–10], as well as volume growth rate during a time period [11, 12]. While a fast growth rate usually indicates malignancy, the outcome requires sufficient time for the growth, more CT scans, and accurate image segmentation for the nodule volumes at two or more time points. Although the geometry related features from the CT images have played an important role for the differentiation task [13–19], texture features have gained great attention for lung CADx [20–23] in recent years. We summarize these recently reported image features and their performance levels in Appendix, where their used datasets are also included.

This work aims to provide a systematic investigation on three widely used types of two-dimensional (2D) texture features, namely the Haralick [24], Gabor [25], and local binary pattern (LBP) [26] features, using the largest public database founded by the Lung Image Database Consortium and Image Database Resource Initiative (LIDC-IDRI) [27]. Specifically, we intend to explore (1) what are the differences of these 2D texture features on differentiating the nodules, (2) how sensitive are these texture features for classification of nodule volume data with different image thicknesses or data acquisition protocols, and (3) whether these texture features have a high possibility on distinguishing the nodules in a reasonably large database. Based on the outcome of the above investigation, we further study how the three-dimensional (3D) expansion will impact the differentiation task. As the feature dimension increases from 2D to 3D space, we further investigate how the reduction of feature dimension will affect the differentiation task. We expect that this systematic investigation will generate the knowledge on the capacity of the widely used texture features and their variations and further render a base on which we can measure the gain by adding any new features.

The remainder of this paper is organized as follows. In "Materials," the utilization of the downloaded LIDC-IDRI database is described. In "Three Types of Texture Features and Their Calculation Methods," the foundations and principles of the three types (Haralick, Gabor, and LBP) of texture features are presented, followed by description of 3D expansion. In "Experimental Design and Results," the evaluation experiments are designed, and the results are reported. Finally, discussions and conclusions are given in "Discussion and Conclusion."

Materials

In this section, the preprocessing of the CT image volume data of pulmonary nodules from the LIDC-IDRI database is introduced by the following two subsections.

- A brief description of the lung image database with painting outlines of the nodules by up to four radiologists ("Lung CT Image Database").
- Automatic extraction of all the nodules volumes from the pulmonary CT images by combining all the radiologists' painting boundaries ("Extraction of Nodule Volumes").

Lung CT Image Database

The lung CT images used in this paper were downloaded from the online resource named LIDC-IDRI [27], which was initiated by the National Cancer Institute (NCI), further advanced by the Foundation for The National Institutes of Health (FNIH), and accompanied by the Food and Drug Administration (FDA). The LIDC-IDRI Database is the largest public resource of lung nodules in the world, which contains 1,012 patient cases, each case includes images from a clinical thoracic CT scan and an associated XML file that records the locations of the pixels on the nodule boundary in each image slice and nine characteristics of the nodule detected by up to four experienced thoracic radiologists. These images were scanned by a wide range of different scanner manufacturers with different image slice thicknesses, such as 0.60, 0.75, 0.90, 1.00, 1.25, 1.50, 2.00, 2.50, 3.00, 4.00, and 5.00 mm. Therefore, the LIDC-IDRI Database is becoming an essential medical imaging research resource to spur the development of computer-aided nodule detection (CADe), segmentation (CADseg), and diagnosis (CADx), validation of various proposed methodologies, and dissemination in clinical practice.

According to the rules of constructing the LIDC-IDRI database, the malignancy assessments are defined in five levels, i.e., 1, 2, 3, 4, and 5, from benign to malignant. Among them, "3" means the malignancy of the corresponding nodule is uncertain. Therefore, the nodules with label "3" were treated in two different ways in this study: (i) they were grouped into those nodules labeled "1" and "2" as benign class; (ii) they were grouped into those nodules labeled “4” and “5” as malignant class.

Extraction of Nodule Volumes

Because the boundaries of each nodule on each CT slice were drawn by up to four radiologists independently, the candidate nodule volume formed by each area on each CT slice was extracted as the combinations of the up-to-four outlines with the references of the associated XML files. For the evaluation purpose, only those nodules with three or four radiologists’ assessment were considered in the following. The combination rule of the four outlines for each slice of each nodule is to extract all image pixels inside their painting boundaries and select the intersection area of at least three radiologists’ decisions as the nodule’s region in an image slice. Stocking those associated image slices together gives the nodule volume. The algorithm of extracting the nodule volume data is outlined as follows.

Algorithm 1: Nodule Volume Extraction

```
1) Read all the pixels belong to the four boundaries of each nodule.
2) Fill the inner pixels for each of the four boundaries.
3) Calculate the times ($t_n$) of each pixel being contained by the four boundaries.
4) Label the inner pixels by combination times.
    If ($t_n \geq 3$)
        The pixel is labeled.
5) Combine all the labeled pixels, and then extract the nodule volume data from the CT images
   according to their spatial coordinates.
```

As an example, the combination processing of a sample nodule on a CT image is shown in Fig. 1.

After the volume of a nodule was determined from the radiologists’ drawings, the volume was then translated into the corresponding image volume by the use of the associated annotation file, named “imageZposition,” which is included in the XML files (i.e., a part of the LIDC database) and provides the slice information where each nodule’s boundaries were drawn by the radiologists. Once the volume of a nodule was identified in the corresponding image volume, the image volume data of that nodule was then obtained. From the image volume of a nodule, various geometric and texture features can be extracted. Extraction of the texture features is presented below.

Three Types of Texture Features and Their Calculation Methods

Three types of widely used 2D texture features (Haralick, Gabor, and LBP) and their calculation methods are introduced in this section. Expansion to 3D space is described using the 2D Haralick feature type as an example, where the reduction of feature size or dimension is illustrated by the principal component analysis (PCA) [28].

- 2D Haralick features calculation method based on the gray-tone spatial-dependence matrices (GTSDMs) (“Feature Extraction Based on 2D Gray-Tone Spatial-Dependence Matrices”).
- 2D Gabor features calculation based on Gabor filters (“Feature Extraction Based on Gabor Filters”).
- Calculation of the statistical LBP features expressed by the local binary patterns (“Feature Extraction Based on Local Binary Patterns”).
- 3D Haralick features calculation methods based on the 3D GTSDMs (“3D Expansion of Haralick Feature Models on Gray-Tone Spatial-Dependence Matrices”).
- PCA algorithm applied on 2D and 3D Haralick features (“Principal Component Analysis on the Haralick Feature Vector Space”).

Feature Extraction Based on 2D Gray-Tone Spatial-Dependence Matrices

This feature extraction method assumes that the texture information of a nodule is contained in the extracted nodule image volume I [24]. In other words, the texture information can be adequately specified by a set of GTSDMs, which are computed for various angular relationships and distances between neighboring resolution cell pairs on each of the image slices. Then, the texture features are calculated from the analyzed statistics or pattern matrices. There are two steps to obtain the texture features using this method, namely, (i) generation of GTSDMs and (ii) feature extraction from these matrices. The algorithm of extracting the texture features is outlined as follows.

Algorithm 2: 2D Haralick Features Calculation

```
1) Quantize the gray value of each pixel to $N_g$ levels.
2) Generate the pattern matrices on all of the four directions, 0°, 45°, 90°, and 135°.
3) Calculate 14 Haralick features from each pattern matrix on each direction separately for four directions in total.
4) Calculate the mean and range of each feature over the four directions.
```

In algorithm 2, suppose the image to be analyzed is rectangular in a 2D representation, the resolution is $N_x \times N_y$, and the gray value of each image pixel is quantized into N_g levels. The distance of the neighbor points on each direction is 1 pixel unit. For each pixel in the image, the correlations between the eight neighbor pixels and itself are described in four directions, such as 0°, 45°, 90°, and 135°. An illustrative drawing is shown in Fig. 2.

For each direction, a GTSDM can be calculated according to the gray value combinations of the neighbor and the central pixels, which are shown in Table 1. # (i, j) $(i, j=1, 2, \ldots, N_g)$ stands for number of times gray tones i and j have been as neighbors. Therefore, the resolution of each GTSDM is $N_g \times N_g$.

The basic assumption in the extraction method above is that all the texture information is contained in gray-tone spatial-dependence matrices. Therefore, all textural features can be extracted from the matrices. A set of 14 measures of texture features are usually calculated, such as angular second moment, contrast, correlation, sum of squares (variance), inverse difference moment, sum average, sum variance, sum entropy, entropy, difference variance, difference entropy, information measures of correlation, and maximal correlation coefficient. The formulas of these texture features have been given in [24]. There are 14 features on each direction. Because this feature calculation method was proposed by Robert M. Haralick [24], the 14 texture features are then named as Haralick features in the literature.

After the feature values are calculated along all four directions, the mean and range of each feature can be averaged over the four directions, resulting in a set of 2×14 features in total to classify each nodule. In this paper, 2D Haralick features were extracted according to two different rules: (1) from the single CT image slice, which contains the largest area of the candidate nodule and (2) from all the CT image slices, which contain the parts belonging to the candidate nodule.

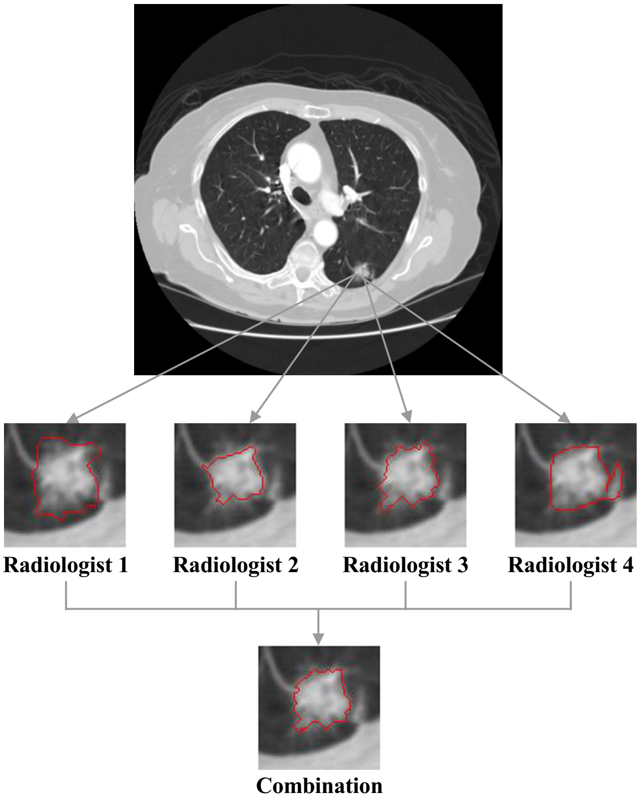

Fig. 1 The combination processing of one nodule based on the paintings from four radiologists

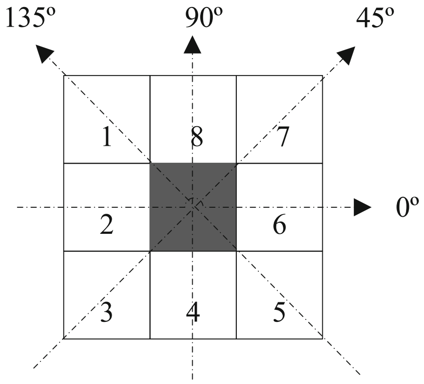

Fig. 2 Pixels 2 and 6 are 0° nearest neighbors to the central pixel, pixels 3 and 7 are 45° nearest neighbors, pixels 4 and 8 are 90° nearest neighbors, and pixels 1 and 5 are 135° nearest neighbors

Table 1 General form of any GTSDM for any direction

Gray level	1	2	3	…	N_g
1	#(1, 1)	#(1, 2)	#(1, 3)	…	#(1, N_g)
2	#(2, 1)	#(2, 2)	#(2, 3)	…	#(2, N_g)
3	#(3, 1)	#(3, 2)	#(3, 3)	…	#(3, N_g)
…	…	…	…	…	…
N_g	#(N_g, 1)	#(N_g, 2)	#(N_g, 3)	…	#(N_g, N_g)

Feature Extraction Based on Gabor Filters

Gabor functions were first proposed by Dennis Gabor for communication applications in 1946 [25]. Since then Gabor functions have been deployed in many areas of signal processing. In the image processing field, Gabor functions are usually used as Gabor filters for multi-dimensional signal processing applications [29]. In particular, as a texture feature extractor, Gabor filters are becoming a widely used method in recent years.

A Gabor filter is obtained by modulating a sinusoid with a Gaussian functional and further being discretized over orientation and frequency [30]. 2D Gabor filters can be defined as follows in the spatial domain (x, y):

$$g(x,y;\lambda,\theta,\phi,\sigma,\gamma)=\exp\left(-\frac{x'^2+\gamma^2y'^2}{2\sigma^2}\right)\exp\left(i\left(2\pi\frac{x'}{\lambda}+\phi\right)\right) \quad (1)$$

$$x'=x\cos\theta+y\sin\theta \quad (2)$$

$$y'=-x\sin\theta+y\cos\theta \quad (3)$$

where the arguments x and y specify the position of a light impulse in the visual field, λ, θ, ϕ, σ, and γ are parameters [31]. λ represents the wavelength of the sinusoidal factor, and the spatial frequency can be shown as $1/\lambda$. θ ($\theta\in[0,\ \pi)$) represents the orientation of the normal to the parallel stripes of a Gabor function. ϕ ($\phi\in(-\pi,\ \pi]$) is the phase offset. Since the nodules are usually circular-shaped, we chose $\phi=0$ for symmetric receptive fields. σ is the sigma parameter of the Gaussian envelope, which can be determined by λ. σ/λ is a constant value empirically set, and then σ can be determined by λ. γ is the spatial aspect ratio that specifies the ellipticity of the support of the Gabor function. It has been found to vary in a limited range of $0.23<\gamma<0.92$ [32]. In this paper, the value of γ is used as 0.92. Finally, only the parameters θ and λ are used to index a Gabor filter function.

The response of a Gabor filter to an image is obtained by a 2D convolution operation. An input image $I(x,y)$, $x,y\epsilon\ \Omega$, (Ω, the set of image points), is convolved with a 2D Gabor function, $g(x,y,\ \lambda,\ \theta,\ \psi,\ \sigma,\ \gamma)$, $x,y\epsilon\ \Omega$, to obtain a Gabor feature image $r(x,y)$ as follows:

$$r(x,y)=\iint_{\Omega} I(\xi,\eta)g(x-\xi,y-\eta;\lambda,\theta,\psi,\sigma,\gamma)\mathrm{d}\xi\mathrm{d}\eta \quad (4)$$

In this paper, the parameter values (orientation θ=0°, 45°, 90°, 135° and frequency $1/\lambda$=0.3, 0.4, 0.5) were adopted according to the experiences referred to [10]. As mentioned in that paper, the mean and standard deviation of each Gabor response image were calculated to be the features for our classification purpose. The feature extraction algorithm is outlined as follows.

Algorithm 3: Gabor Features Calculation

```
1) Input 2D image slices of the candidate nodule.
2) Set parameters $\theta$ (0°, 45°, 90°, and 135°) and $1/\lambda$ (0.3, 0.4, and 0.5) of Gabor filters.
3) Get the response images from the convolution of 2D images and each Gabor filter separately.
4) Calculate the mean and standard deviation values of response images for the candidate nodule
   according to each Gabor filter.
```

Feature Extraction Based on Local Binary Patterns

As a model of texture analysis based on the so-called texture unit, local binary pattern or LBP was first introduced in [26, 33]. The main idea is that a texture image can be characterized by its texture spectrum in the image. The LBP calculates the relationships between each neighborhood pixel and the central one and describes textures based on the histogram of the whole region of interest. Because of the advantage on the powerful illumination invariant, LBP has been widely recognized as a texture operator. This LBP texture operator has been highly successfully used for various computer vision applications, especially for face recognition [34].

Many favorable patterns were proposed based on different numbers of neighborhood pixels with different radii around the central pixel. However, the basic LBP operator introduced as a standard example and used mostly in practices is based on the eight neighbor pixels [35]. An illustration for the basic LBP operator is shown in Fig. 3.

The relationships of the central pixel P_c and the surrounding pixels P_n (n=0, 1, …, 7) on gray levels are calculated by:

$$s(x) = \begin{cases} 1 & x \geq 0 \\ 0 & \text{otherwise} \end{cases}, x = P_n - P_c \tag{5}$$

If the gray value of a neighbor pixel is higher than or equal to that of the central one, the value of $s(x)$ is set to 1, otherwise to 0. The descriptor describes the result over the neighborhood as a binary pattern as follows:

$$\mathrm{LBP}_{R,N}(x,y) = \sum_{i=0}^{N-1} s(P_i - P_c) \times 2^i \tag{6}$$

where N is equal to eight in this illustrative example, P_c value corresponds to the gray value of the central pixel of a local neighborhood, and P_i to the gray values of N equally spaced pixels on a circle of radius R. Therefore, the signs of the differences in a neighborhood are interpreted as an N-bit binary number, resulting in 2^N (e.g., 2^8=256) distinct values for the binary pattern. However, many images of a nodule or other objects cannot contain all 256 patterns. Therefore, the selection of effective patterns should be adopted in most applications. The feature extraction algorithm is outlined as follows.

Algorithm 4: LBP Features Calculation

```
1) Input 2D image slices of the candidate nodule.
2) Calculate eight patterns of each pixel in one 2D image except the boundary points (the boundary
   points are not belong to the candidate nodule).
3) Calculate the statistical probabilities of each pattern in the whole 2D image.
4) Summarize the statistical probabilities of each pattern on all of the images containing the current
   nodule as LBP feature candidates.
```

3D Expansion of Haralick Feature Models on Gray-Tone Spatial-Dependence Matrices

While 2D medical images of axial cross-section can always give rich information for various clinical tasks, there is a conjecture that more information can be obtained in 3D image space. Therefore, the 3D texture features extracted from the 3D volume nodule data were considered. As an example, we designed and implemented a calculation model based on the 2D model to obtain the 3D Haralick features [36–38].

The integral part of our idea is to regard the volume as a structure, which consists of many spatial texture elements.

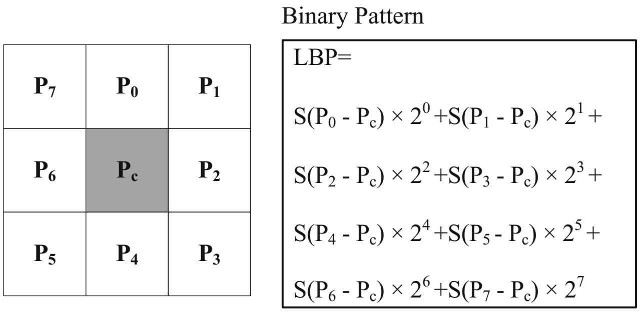

Fig. 3 Typical LBP features based on a neighborhood of eight pixels

Following the same calculation procedure as that on 2D image, we can apply the calculation model of Haralick features to 3D gray-level volume data. In 2D images, there are eight neighbor pixels around the central one with the distance of one pixel. In 3D space, each voxel has 26 neighbors with distance of one voxel (d=1). Therefore, there are 13 directions in the 3D model (shown as in Fig. 4) for the calculation of Haralick features. For each direction, 14 texture features can be calculated from the corresponding GTCM. Therefore, more directions and space information are considered.

To study the contributions of different directions for the classification of lung nodules, we designed three different combination modes of directions, which contain 5, 9, and 13 directions, respectively. The standard rule for different combinations of 3D directions is based on the spatial distances between the neighboring voxels and the central one. The first combination contains A_1, A_2, A_3, A_4, and A_{13}; the second combination contains A_1, A_2, A_3, A_4, A_5, A_7, A_9, A_{11}, and A_{13}; and the third combination contains all of the 13 directions shown in Fig. 4. The schematic diagram of the three combinations of directions studied in this paper is shown in Fig. 5.

Suppose H_{ij} is the jth (j=1, 2, …, 14) texture feature value in the ith direction (i=1, 2, …, n, n=5, 9, 13) calculated from

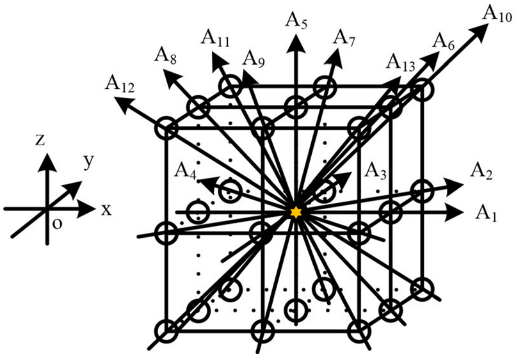

A₁ = (0°, 0°, 0°);
A2 = (45°, 0°, 0°);
A3 = (90°, 0°, 0°);
A4 = (135°, 0°, 0°);
A5 = (0°, 90°, 90°);
A6 = (0°, 0°, 45°);
A7 = (90°, 45°, 90°);
A8 = (0°, 90°, 135°);
A9 = (90°, 135°, 90°);
A10 = (45°, 45°, 45°);
A11 = (135°, 45°, 135°);
A12 = (45°, 135°, 135°);
A13 = (135°, 135°, 45°).

Fig. 4 The 3D resolution cells for one center voxel in 13 directions. The angular A_i (i=1, 2, …, 13) is equal to (θ_{xy}, θ_{yz}, θ_{xz}). θ_{xy} is the angle between the project vector on x–y flat and x-axis, θ_{yz} is the angle between the project vector on y–z flat and y-axis, and θ_{xz} is the angle between the project vector on y–z flat and z-axis

the GTCMs proposed by Haralick, the final Haralick features should be 2×14=28, which contain the mean and range of the texture feature values on the directions of different combination modes. The formulas can be shown as follows.

$$\mathrm{Mean}_{jn} = \frac{1}{n}\sum_{i=1}^{n} H_{ij} \tag{7}$$

$$\mathrm{Range}_{jn} = \max_{i=1\ldots n}\{H_{ij}\} - \min_{i=1\ldots n}\{H_{ij}\} \tag{8}$$

However, the physical distance between the neighbor voxels along z axis is usually different from x and y axis. Therefore, when we use the 3D Haralick feature model, we should pay attention to the different physical distances of neighbor voxels along different axis [38]. If the volume data is anisotropic, it may need to do resampling operation. The outline of calculating 3D Haralick features is shown as follows.

Algorithm 5: 3D Haralick Features Calculation

1) Resample the anisotropic volume data to isotropic one.
2) Quantize the gray value of each pixel to N_g levels.
3) Generate the GTCMs on all of the thirteen directions in the 3D volume model.
4) Calculate 14 Haralick features from each GTCM on each direction separately for the thirteen directions in total.
5) Calculate the mean and rang of each feature over the five, nine, and thirteen directions.

Principal Component Analysis on the Haralick Feature Vector Space

After calculation of the Haralick features, each sample has a feature vector containing 28 factors. When combining the texture features to other features (size, shapes, etc.), the dimension of the texture feature vector, however, can be very large. PCA algorithm is a popular mathematical procedure that uses orthogonal transformation to convert a set of observations of possibly correlated variables into a set of values of linearly uncorrelated variables called principal components (PCs) [28]. Therefore, it was used in our study to reduce the number of texture features without much efficiency reduction. Other application can be seen in [39].

Suppose there are n samples, the resolution of the feature matrix formed by the feature vectors is n×28. According to the principle of PCA algorithm [28], feature vectors in the feature matrix are transformed to an equal number of principal components and the corresponding scores. Then, we rank the scores and corresponding principal components based on the values of scores decreasingly. The cumulative energy content of the ith (i=1, 2, …, 28) component is the sum of the former i scores divided by the sum of all scores. Finally, the principal components can be selected as the new feature vectors by the firstly setting of the cumulative energy content.

Experimental Design and Results

Data Preparation

A major purpose of this study is to evaluate the efficiencies of different texture features for classification of malignant and benign lung nodules. For this purpose, the entire LIDC database, which is so far the largest public database available, was utilized. While all the images were acquired with equal pixel size in each image slice, the image thickness varies, depending on data

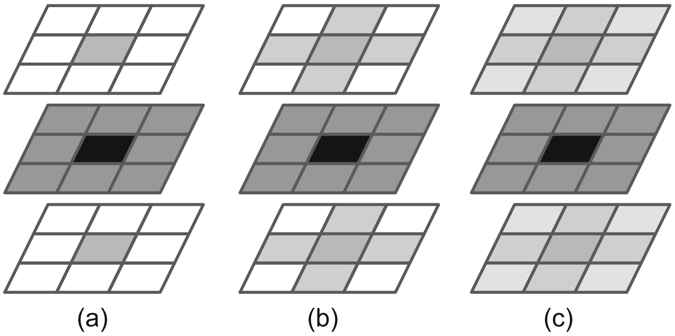

Fig. 5 Three combination modes of the neighbor voxels on 3D directions. **a** Combination of five directions, **b** combination of nine directions, **c** combination of 13 directions

acquisition protocols. Investigation on the dependence of the features on the image thickness is one task of this work. As described in "Materials," in the LIDC-IDRI database, the radiologists' malignancy assessments are labeled as "1," "2," "3," "4," and "5" levels. Figure 6 shows the nodules (diameter>3 mm) of the database in terms of image thickness and class labels used in our experiments. The vertical axis shows the number of nodules.

In this study, we grouped "1" and "2" as benign class, "4" and "5" as malignant class, and "3" as uncertain class. The label "3" or uncertain class can be treated in two different scenarios. In the first scenario, "3" was grouped into benign class. In the second scenario, "3" was grouped into malignant class.

By inputting the extracted features from the 1,356 nodules (of three thickness groups) and the labels of two classes (1=malignance and 0=benign) into the well-known support vector machine (SVM) with the widely used kernel of radial basis function (RBF) [40], we randomized the training and testing process for 100 times. The corresponding 100 classification outcomes of sensitivity and specificity were obtained. From each set of 100 classification outcomes of an image slice thickness, the mean and standard deviation measures were computed. The following sections present the study design and experimental outcomes.

Comparison of Three Types of 2D Texture Features Based on Different Slice Thicknesses

Based on the description of the three texture features in "Three Types of Texture Features and Their Calculation Methods" above, 28 Haralick features, 24 Gabor features, and 256 LBP features were extracted from the segmented volume data of each nodule. In extracting the Haralick features, 14 measures of the four directions (0°, 45°, 90°, and 135°) were calculated, but when calculating the maximal correlation coefficient feature, it cost too much time. Therefore, there were 13 measures left, which can be evaluated on each direction in this study. Then, the Haralick features were presented by the mean and range values of the 13 measures over the four directions, resulting in a total of 26 features (i.e., 13×2). For the parameters of Gabor filters, according to the previous research reports [29–32], we selected the same directions as mentioned above of 0°, 45°, 90°, and 135° and the frequencies of 0.3, 0.4, and 0.5, resulting in a total of 24 features. By theory, a total of 256 LBP features would be extracted. However, in our situation, most of the feature values were zero. This indicates that most patterns are not existed in the nodule CT images. All of the features were undergone a principal component analysis, and 0.9985 of cumulative probability was empirically selected. This resulted in 40±5 LBP features as input to the SVM classifier.

The first experiment was performed on the original data of different image slice thicknesses. Three image groups were selected from the LIDC-IDRI database: Group 1 (Data_250) has 630 nodules of 2.50±0.50 mm image thickness, group 2 (Data_125) has 330 nodules of 1.25 and 1.50 mm thickness, and group 3 (Data_100) has 396 nodules of 1.00 mm thickness or less. Those nodules of image thickness beyond 4.00 mm were ignored.

The outcome from the first scenario, where the label "3" was grouped into benign class, is shown by Fig. 7. Each receiver operating characteristics (ROC) plot was drawn from the SVM classification of the features from all the nodules. The mean and standard deviation (SD) values of the area under the ROC curve (AUC) measures are shown in Table 2.

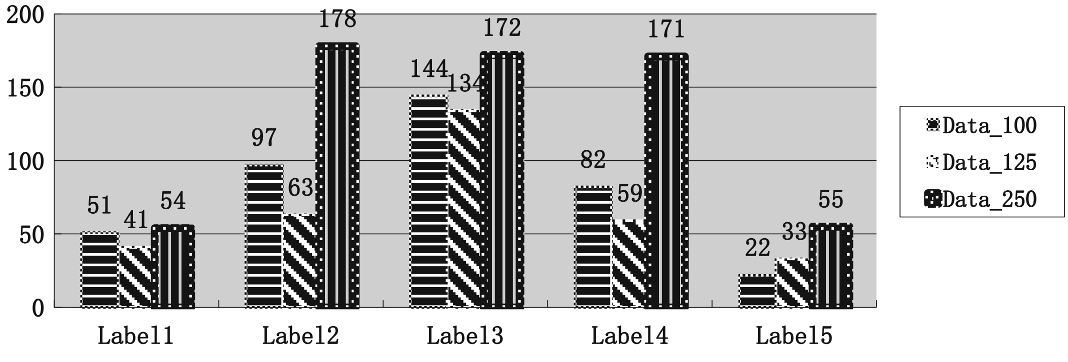

Fig. 6 The information about class labels and image thickness in the LIDC-IDRI database used in this study

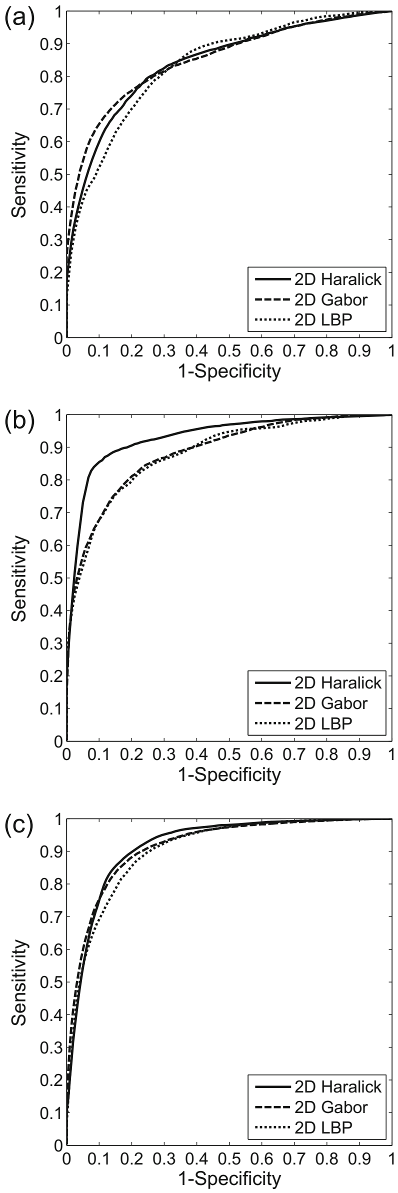

Fig. 7 The ROC curves of the three types of texture features' classification performance on the three groups of different image thickness nodule data. **a** ROC curves of three types of features applied on the nodule data with 1.00 mm or less slice thickness. **b** ROC curves of three types of features applied on the nodule data with 1.25 and 1.50 mm slice thickness. **c** ROC curves of three types of features applied on the nodule data with 2.50±0.50 mm slice thickness

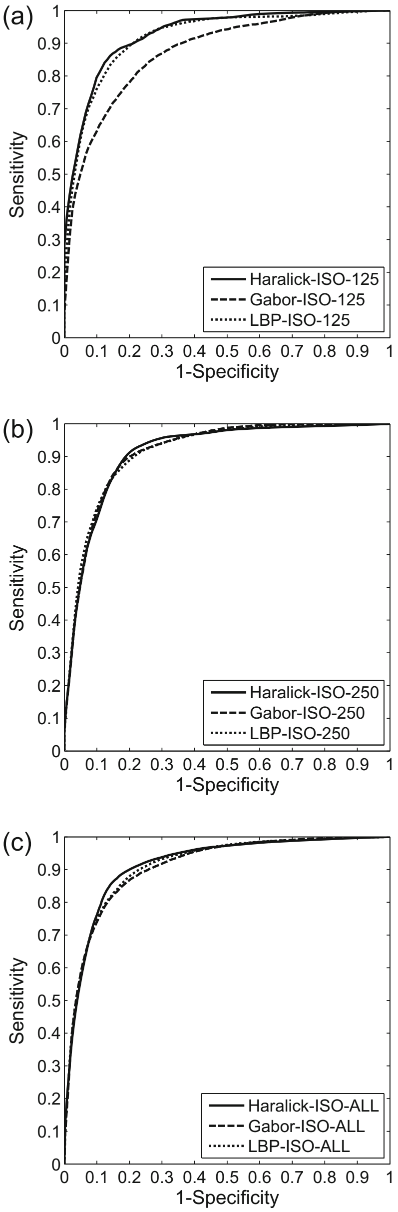

Fig. 8 The ROC curves of the three types of texture features' classification performances on the interpolated image data. **a** ROC curves from the interpolated 1 mm data from 1.25 mm thickness. **b** ROC curves from the interpolated 1 mm data from 2.50 mm thickness. **c** ROC curves from the combination of all the interpolated data and the original Data_100 datasets

Table 2 The AUC information about the performances of the three types of texture features

AUC information	Haralick features		Gabor features		LBP features	
	Mean	SD	Mean	SD	Mean	SD
Data_100	0.8393	0.0491	0.8485	0.0413	0.8321	0.0230
Data_125	0.9270	0.0257	0.8805	0.0437	0.8779	0.0232
Data_250	0.9160	0.0150	0.9139	0.0116	0.9022	0.0171
Average	0.8941	0.0299	0.8810	0.0322	0.8707	0.0211

Table 3 The AUC measures on different texture features from the three types of interpolated image data

AUC information	Haralick features		Gabor features		LBP features	
	Mean	SD	Mean	SD	Mean	SD
Data_125 (interpolated)	0.9256	0.0256	0.8699	0.0310	0.9166	0.0200
Data_250 (interpolated)	0.9113	0.0179	0.9130	0.0149	0.9126	0.0126
Data_100+ Data_125 (interpolated) + Data_250 (interpolated)	0.9124	0.0120	0.9083	0.0099	0.9119	0.0096

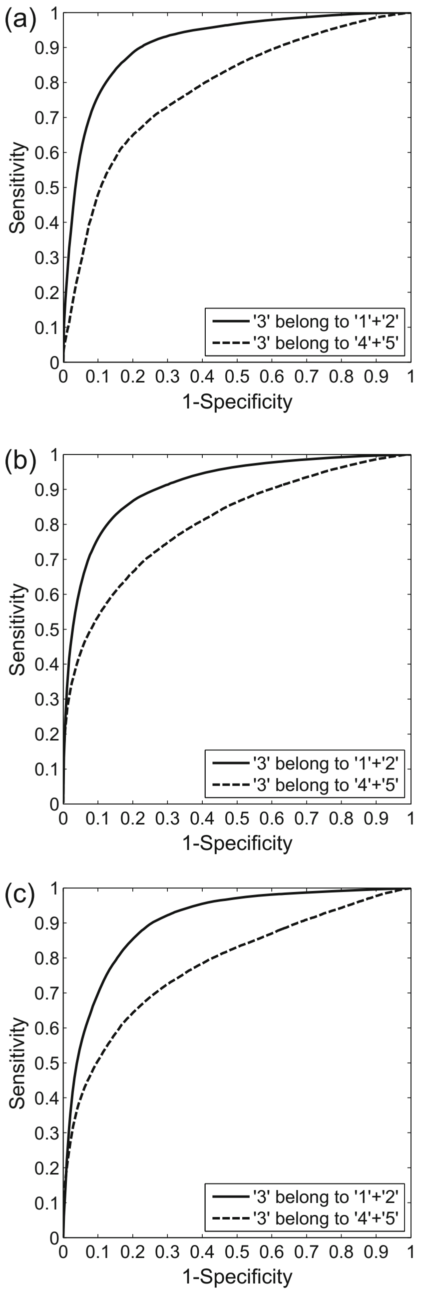

Fig. 9 The ROC curves of the three types of texture features' classification performances on the two scenarios. **a** ROC curves on the Haralick features from the two scenarios. **b** ROC curves on the Gabor features from the two scenarios. **c** ROC curves on the LBP features from the two scenarios

A high effectiveness of the three types of 2D texture features on the classification of malignancy can be visualized in Fig. 7 and also reflected by the average mean and standard deviation values of the AUC measures as listed in Table 2. The classification results from the Haralick features have shown significantly higher AUC values in average on Data_125 group (*t* test p value$_{\mathrm{HG}}$=1.1102×10^{-16}, p value$_{\mathrm{HL}}$=5.6431×10^{-32}) and Data_250 group (*t* test p

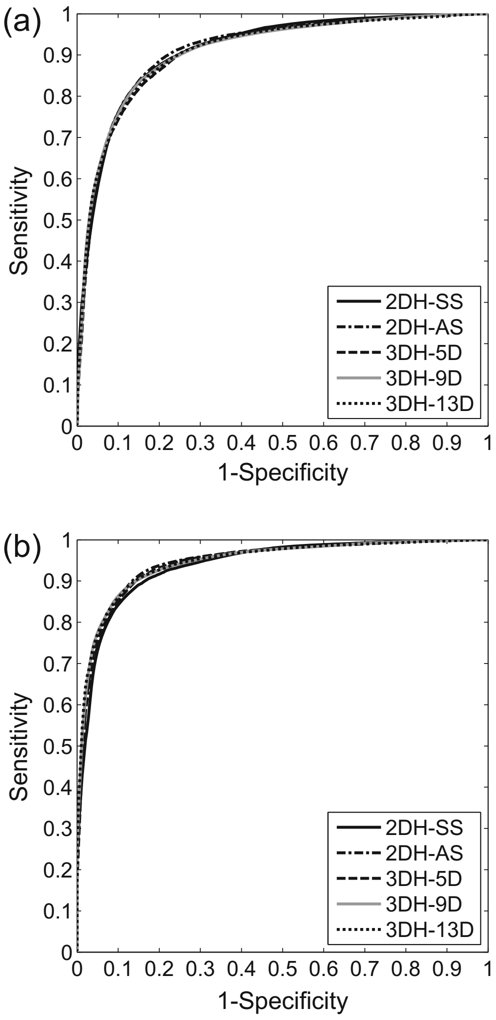

Fig. 10 The ROC curves of the 2D and 3D Haralick texture features' classification performances from the two experiments. **a** Classification performances on the dataset containing the uncertain nodules (i.e., the nodules labeled by "3"). **b** Classification performances on the dataset without the uncertain nodules

Table 4 The AUC measures on the three types of texture features from the two scenarios

AUC information	Haralick features		Gabor features		LBP features	
	Mean	SD	Mean	SD	Mean	SD
“3” belong to “1”+“2”	0.9124	0.0121	0.9101	0.0112	0.9012	0.0097
“3” belong to “4”+“5”	0.7810	0.0266	0.8045	0.0212	0.7799	0.0127

Table 5 The AUC measures for the performances of the 2D and 3D Haralick texture features from the two experiments

AUC information With label “3” nodules	Mean	Standard D	AUC information Without label “3” nodules	Mean	Standard D
2D Haralick features (single slice)	0.9113	0.0106	2D Haralick features (single slice)	0.9373	0.0103
2D Haralick features (all slices)	0.9124	0.0121	2D Haralick features (all slices)	0.9432	0.0109
3D Haralick features (5 directions)	0.9069	0.0103	3D Haralick features (5 directions)	0.9426	0.0088
3D Haralick features (9 directions)	0.9086	0.0124	3D Haralick features (9 directions)	0.9440	0.0100
3D Haralick features (13 directions)	0.9080	0.0110	3D Haralick features (13 directions)	0.9441	0.0088

Table 6 *t* test results of the 2D and 3D Haralick features on the data with the uncertain nodules (labeled by “3”)

P-value	2DH of single slice	2DH of all slices	3DH of 5 directions	3DH of 9 directions	3DH of 13 directions
2DH of single slice		0.4972	0.0034	0.1103	0.0319
2DH of all slices	0.4972		6.9789×10^{-4}	0.0336	0.0079
3DH of 5 directions	0.0034	6.9789×10^{-4}		0.2752	0.4741
3DH of 9 directions	0.1103	0.0336	0.2752		0.6807
3DH of 13 directions	0.0319	0.0079	0.4741	0.6807	

Table 7 *t* test results of the 2D and 3D Haralick features on the data without the uncertain nodules (labeled by “3”)

p value	2DH of single slice	2DH of all slices	3DH of 5 directions	3DH of 9 directions	3DH of 13 directions
2DH of single slice		1.0576×10^{-4}	1.3072×10^{-4}	5.9170×10^{-6}	2.4057×10^{-6}
2DH of all slices	1.0576×10^{-4}		0.6528	0.6106	0.5253
3DH of 5 directions	1.3072×10^{-4}	0.6528		0.3003	0.2352
3DH of 9 directions	5.9170×10^{-6}	0.6106	0.3003		0.9019
3DH of 13 directions	2.4057×10^{-6}	0.5253	0.2352	0.9019	

Table 8 The cumulative energy content of the former PCs from 2D and 3D Haralick features

No. of PCs	1	2	3	…	9	…	26
2D Haralick features (single slice)	0.998511	0.999515	0.999863	…	1.000000	…	1.000000
3D Haralick features (13 directions)	0.991478	0.997637	0.999096	…	1.000000	…	1.000000

Table 9 The AUC information about the performances of 3 PCs, 9 PCs, and 26 PCs after PCA analysis on the 2D and 3D Haralick features

AUC information	2D Haralick features (single slice)		3D Haralick features (13 directions)	
	Mean	Standard deviation	Mean	Standard deviation
3 PCs	0.8354	0.0151	0.8814	0.0131
9 PCs	0.8849	0.0137	0.8978	0.0130
26 PCs	0.9377	0.0095	0.9386	0.0093

value$_{HG}$=0.2601, p value$_{HL}$=6.3565×10^{-9}) than that of the Gabor and LBP features. For Data_100 group, all three types of features showed similar performance. Because of the large database and 100 repeated runs, the above experimental outcome would lead to the following conclusion: While the three types of texture features performed similarly for noisy data (thinner image slices), the Haralick features outperformed the other two types as the image noise level goes down (thicker image slices). When the image slice thickness goes beyond 3.0 mm, image details along the slice direction will be averaged out and the details in the axial cross-section will be affected by partial volume effect, no obvious gain is expected. This conjecture is demonstrated by the outcome from the Haralick features. To further investigate the influence of image slice thickness on the classification performance, we conducted another experiment below.

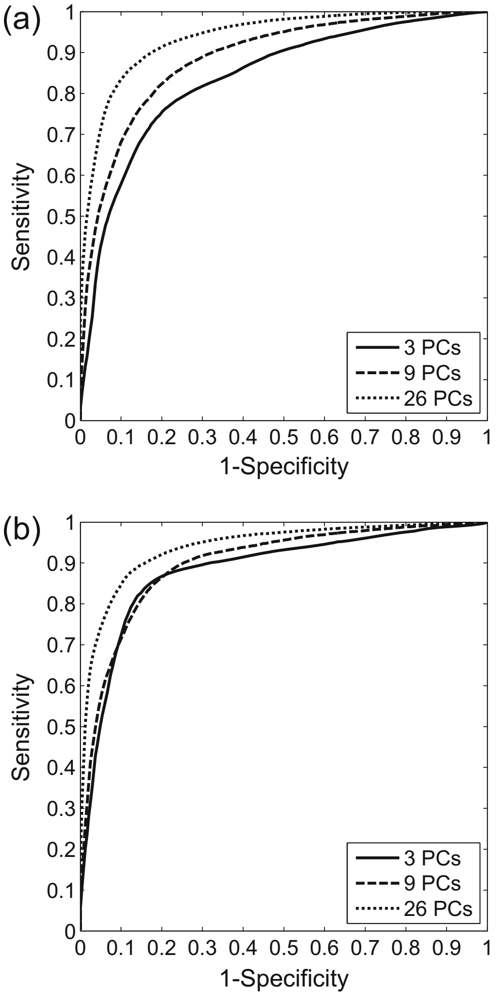

Fig. 11 The ROC curves of the classification evaluates based on 3, 9, and 26 PCs extracted from the 2D and 3D Haralick features. **a** Different PCs from 2D Haralick features of single slices. **b** Different PCs from 3D Haralick features of volume data formed by all slices

Comparison of Different 2D Texture Features after Thickness Interpolation

In this experiment, we interpolated the thick images to a same thinner thickness. The interpolation method used here is referring to a cubic interpolation algorithm mentioned in [41].

Because the pixel sizes in the cross-section CT images are all smaller than 1 mm, we only interpolated those nodule volume data whose thicknesses are >1 mm, such as the Data_125 and Data_250. A total of 960 nodule datasets were interpolated into 1-mm slice thickness. The other 396 nodule datasets in Data_100 were remained. Then, the three types of texture features were extracted from the interpolated and remained datasets, namely, the (axially) isotropic volume data. The extracted features were then compared by the same methods described in "Data Preparation." The averaged outcomes are plotted as ROC curves in Fig. 8. The statistical information of the ROC curves or AUC measures are shown in Table 3.

Based on the results of Figs. 7 and 8 as well as Tables 2 and 3 above, the following observations can be documented: (1) The 2D Haralick texture features have higher mean values of the AUC measures on the isotropic data than the Gabor and LBP features (t test p value$_{HG}$=0.0100, p value$_{HL}$=0.7901); (2) by comparing the classification results on the anisotropic and isotropic data, the interpolation did not show noticeable gain for both Haralick and Gabor features; however, the t test results showed some gain for the LBP features (p value$_{HD125}$=0.6998, p value$_{HD250}$=0.0452, p value$_{GD125}$=0.0493, p value$_{GD250}$= 0.6434, p value$_{LD125}$=0.0000, p value$_{LD250}$=1.8905×10^{-6}). Based on the above two observations (more specifically on the improvement for LBP features' performance), the isotropic data were used in the next few experiments below to further investigate the performances of the three types of texture features.

Comparison of Different Experimental Designs on the Uncertain Nodules

The above experiments were performed for the first scenario of grouping the uncertain label "3" into the benign class. The following experiment was performed for the second scenario of grouping the uncertain label "3" into the malignant class. The experiment was performed on the isotropic data as described in "Comparison of Three Types of 2D Texture Features Based on Different Slice Thicknesses." The classification evaluation results of the second scenarios are described by the ROC curves as shown in Fig. 9, where the results of the first scenario are also listed in Table 4 for comparison purpose.

Based on the evaluation experiments of the uncertain nodules with label "3," we can conclude that the uncertain nodules are more similar to the benign ones according to the experts' visual assessment. These experimental outcomes from two different scenarios raise a suspicious that whether the experts' visual assessment might have bias toward classification for benign. Resolving this suspicious requires the ground truth from nodule biopsy, and unfortunately the ground truth is not available.

Because of the advantage performance of the Haralick features over the other two types of features, our next research task is then turned to investigate if there is a gain on expanding the Haralick model from 2D to 3D space.

Comparison of 2D and 3D Haralick Features

The extraction of 3D Haralick texture features was described above in "3D Expansion of Haralick Feature Models on Gray-Tone Spatial-Dependence Matrices." Both 2D and 3D Haralick features were applied to the CT volume images of 1,356 nodules from the LIDC database. All the CT image slice thicknesses were interpolated into 1 mm as unified isotropic data. We calculated the 2D Haralick texture features in two ways: One calculation is from the single slice with the largest area of nodules and the other from all slices containing the nodules. The 3D Haralick features were calculated in three ways: One considered five directions, another considered nine directions, and the third one considered all the 13 directions on the unified isotropic volume data of the nodules. The uncertain nodules with label "3" were considered as the benign ones in one experiment and excluded from the data as another experiment. The classification results of the 2D and 3D texture features from the two experiments are shown in Fig. 10 and Table 5. The ROC curves from both experiments show similar characteristics, indicating that the results are not depending on the data variation. Table 5 shows a gain for 2D features when applied to the 3D data as compared to the outcome from the single 2D image in both experiments. This is expected because more data information about the nodule is used. The gain by the 3D expansion is not seen in terms of AUC mean value from Table 5. To get more insight into the above observations from Fig. 10 and Table 5, we performed more statistical tests below.

To study if the above observations are statistically meaningful, we performed hypothesis *t* test experiments on the 2D and 3D Haralick features on the nodules image data with and without the uncertain nodules of label "3." The *p* values of the outcomes from the test experiments are shown in Tables 6 and 7.

Based on the *t* test experimental results in Tables 6 and 7 as well as AUC measures in Table 5, the following observations can be documented. (i) The 2D Haralick features from the 3D data outperformed the 2D features from the 2D data (with the $p<0.05$) in the absence of the uncertain nodules of label "3" (only the certain labels "1," "2," "4," and "5" were considered), and both performed similarly in the presence of the uncertain nodules (with the $p>0.05$). It seems it is worthwhile to include all the image slices of the 3D data to compute the 2D features because the computing time is not an issue by current desk top computers. (ii) The 3D Haralick features performed slightly better than the 2D Haralick features in the absence of the uncertain nodules because three $p<0.05$ and the other three are >0.05, and did not show gain in discrimination performance on the uncertain nodules because 5 in 6 *p* values of 2D and 3D Haralick features are smaller than 0.05. (iii) The 3D Haralick features from nine directions showed higher discrimination performance than five directions and did not show gain from 13 directions regardless absence or presence of the uncertain nodules. Although the mean value of AUC of 3D Haralick features from 13 directions is the highest (0.9441), it is only 0.0001 higher than the value of 3D Haralick features from nine directions (0.9440) in the absence of the uncertain nodules and the *t* test *p* value is 0.9019>0.05, which means that they are not significantly different. This issue regarding consideration of more or less directions in computing the features seems somehow related to feature redundancy problem in general. In the following, we investigated this redundancy problem by the use of the PCA [28].

Performance of Dimension Reduced 2D and 3D Haralick Features

From the classification results of the above experiments, it was seen that inclusion of the uncertain nodules (labeled by "3") resulted in a noticeable variation in the texture characteristics in both the 2D and 3D space. To avoid the variation, the uncertain nodules were not included in the following study on feature redundancy problem, in more general term the study may be called dimension reduction. Even not including the uncertain nodules, there are still 906 nodules (422 malignant and 484 benign) with certain labels left for this dimension reduction study.

From each lung nodule CT image, total 26 of 3D Haralick texture features were extracted from all the 13 directions. Similarly, total 26 of 2D Haralick texture features were also extracted from the four directions. Given the numbers of the nodules and features, the resolution of the texture feature vector matrix is 906×26. Then, the PCA was applied on the two matrices of 2D and 3D Haralick texture features, respectively. The cumulative energy contents of the ordered principal components were calculated from the eigenvalues which were ranged in descending order. The values are shown in Table 8.

When the number of PCs is 3, all the cumulative energy contents are over 0.999000 according to Table 8. When the number of PCs is 9, all the cumulative energy contents are up to 1.000000. Therefore, we performed two classification experiments, one selected the first three PCs and the other selected the first nine PCs. We also compared the performances of the principal components of 2D vs. 3D Haralick features. The ROC curves and the AUC information of the above reduced features are shown in Table 9 and Fig. 11.

Based on the results from Table 9 and Fig. 11 above, the following observations can be documented. (i) Both 2D and 3D features performed similarly and their performances increased as more PCs were used. This may indicate that the 13 measures from each direction have no significant redundancy. (ii) When recalling the 3D expansion study in "Comparison of Different Experimental Designs on the Uncertain Nodules" above, the redundancy may exist only in the directions involving the *z*-axis, where two factors may be considered when selecting the directions: One is the data sampling rate when CT images are acquired, and the other is the objects' geometry and texture properties along the *z*-axis. For the sampling rate at mm resolution level along the *z*-axis and the nodule sizes also at millimeter level, more than nine directions in the 3D expansion seems not necessary.

Discussion and Conclusion

The effectiveness of three widely used types of 2D (Haralick, Gabor, and LBP) texture features was investigated in this study for CADx purpose of differentiating the lung nodules using the entire LIDC-IDRI CT image database, which is so far the largest one available worldwide. The extraction of these three types of 2D features was implemented in a similar fashion according to their theoretical descriptions. The classification of the extracted features was performed by the well-known SVM classifier with the widely used RBF kernel, which fits our bi-classification task well. The bi-classification outcomes were plotted as ROC curves and further documented quantitatively by the well-established AUC merit on a statistical base, i.e., the mean and standard deviation values of AUC values for 100 repeated times of classification experiments.

For a suggested data acquisition protocol among different CT scanners at a fixed image slice thickness, the three types of 2D features produced similar mean values of the AUC merit. When the image slices increased from <1 mm up to 3 mm, the performance of each type of the features varied to some degree respectively, but the variation is not dramatic. However, the 2D Haralick features had achieved the best result or the highest mean value of AUC merit when the image thickness ranges from 1.25 to 1.50 mm. The gain of the Haralick over the Gabor and LBP features at this thickness range is statistically significant. Their deteriorate performances as the thickness increased over 1.50 mm indicate that thicker than 1.50 mm would not be a choice. Interpolation from a thicker image thickness down to a thinner one (from 3 mm down to 1 mm) did not improve the performance. In other words, the image information content is determined by the originally acquired image, the post-image operation by interpolation does not add more information. Their deteriorate performances as the thickness decreased below 1.25 mm indicate that the image noise can compromise the image information content. In other words, if thinner image thickness is desired for the purpose of improving the performance, then the image noise level must be retained and unavoidably the X-ray radiation risk will increase.

The gain from the 2D Haralick feature type over the other two feature types suggests that the Haralick features might be a preferred choice for further investigations, such as adding more other types of features [42] and improving the classifier [43]. Since the malignancy scores or labels were based on the radiologist experts' visual perception on the image characteristics of the nodules' image slices, the conjecture of the Haralick features being a preferred choice may be translated to a conjecture that the Haralick features may be more correlated to the visual perception.

When the 2D texture features were calculated from the available 3D volumetric data, a noticeable gain was observed as compared to the calculation from a single, largest slice in the 3D data. This observation leads us to conjecture that as isotropic volumetric image data or isotropic voxel size become reality by advanced CT imaging technology, calculation of the 2D textures from the 3D volumetric data has advantage because a higher discrimination performance can be achieved with nearly negligible computing cost by current desktop computers.

Extension of the original theoretical 2D feature model to direct 3D calculation on the 3D data did not show a gain from the LIDC-IDRI image database. Theoretically, the direct 3D calculation on the 3D volumetric data would be beneficial. This open question leads us to explore two directions for further investigation: One is to modify the original 2D feature model to take advantages of the 3D data information. For example, gradient and curvature information are inherently 3D properties of the 3D data and features from the higher order 3D properties could show the benefit [44, 45]. Another direction is to improve the CT image reconstruction for thinner image slices while control the image noise [46, 47].

Since the uncertain nodules rendered a very challenging task for any feature type, we performed a hypothetical test study by neglecting these nodules. The outcome of this test study indicates a potential of obtaining gain by the direct 3D extension or calculation of the 2D model on the 3D volumetric data. While it is straightforward to consider the full 13 directions in the direct 3D calculation in the 3D space, a less number of directions, such as 9, may be beneficial. By the PCA analysis, we found that the feature extraction along each direction does not contain significant redundancy, so an optimal selection of the number of directions may be worth further investigation for other applications.

While the LIDC-IDRI database is the largest public database of lung nodules worldwide and includes the strictly selected CT images of nodules with clear texture information, however, because of the lack of pathological ground truth, the experimental outcomes of this study may have different conclusions when the corresponding pathological ground truth is available. This is an essential limitation of the LIDC-IDRI database. This limitation shall be notified for all investigational efforts in developing CADe, CADseg, and CADx algorithms using the LIDC-IDRI database. But our study show that the texture features of benign and malignant nodules represented in the CT images can be distinguished, and they can be consistent with human visual diagnosis.

Acknowledgments This work was partly supported by the NIH/NCI under grant nos. CA143111 and CA082402, and a PSC-CUNY award 65230-0043. This work was also supported by the National Science Foundation of China under grant nos. 61071213, 61172002, 81071220, and 81230035, the National Key Technologies R&D Program of China under grant no. 2011BAI12B03, the Fundamental Research Funds for the Central Universities under grant no. N120518001, and Liaoning Natural Science Foundation 2013020021.

Appendix

Table 10 Features and their performance levels for nodule differentiation

Scheme	Datasets	Features	Performance level
David F. Yankelevitz et al. in [11]	13 patients	Volume measurement to evaluate the doubling times	All malignant nodules had doubling times of less than 177 days. All benign ones had doubling times of 396 days or longer
Lawrence R. Goodman et al. in [12]	50 nodules, less than 20 mm in diameter, in 29 patients, scanned with 1.25 mm collimation	Volume measurements	The mean inter-observer variability (repeatability) was 0.018 % (SD=0.73 %), and the SD of the mean for 3 contemporaneous scans (reproducibility) was 13.1 % (confidence limits, ± 25.6 %)
Yuichi Matsuki et al. in [4]	155 clinical cases with nodules less than 3 cm (99 malignant and 56 benign nodules)	7 clinical parameters and 16 radiologic findings	The area under the receiver operating characteristic (ROC) curve (Az value) of the artificial neural network alone was 0.951
Giuseppe Cardillo et al. in [5]	429 patients (276 men and 153 women)	Age, diameter, smoking habits, evidence of calcifications, surgical procedure, and history of previous cancer	370 lesions were benign (86.24 %): mean age, 49; mean diameter, 1.8 cm; evidence of calcifications, 43 cases (11.62 %); smokers, 201 cases (54.32 %); history of previous cancer, 11 cases (2.97 %)
Feng Li et al. in [6]	61 malignant and 183 benign nodules	Two clinical parameters (patient age and sex) and 56 features extracted from images (e.g., effective diameter, etc.)	The Az value of the CADx scheme alone was 0.831 for distinguishing benign from malignant nodules
Michael F. McNitt-Gray et al. in [8]	31 cases (14 benign and 17 malignant)	Several quantitative measures were extracted based on each nodule's size, shape, attenuation, distribution of attenuation, and texture	28/31 cases (90.3 %) of the training set were correctly classified
Qiang Li et al. in [9]	415 CT scans (76 confirmed cancers and 413 confirmed benign nodules)	Three features, i.e., effective diameter, degree of circularity, and contrast	The Az value for the average performance of the five radiologists was 0.63 (p<0.01)
Dmitriy Zinovev et al. in [9]	All the labeled nodule data from the Lung Image Database Consortium (LIDC) database [27]	64 two-dimensional (2D) low-level image features grouped into four categories: shape, texture, intensity, and size features	The proposed approach can correctly predict 70 % of the instances contained in the dataset
Ted W. Way et al. in [14]	96 lung nodules (44 malignant, 52 benign) from 58 patients	3D gradient, 3D curvature, mask energy, morphological and gray-level features	The system achieved the Az value of 0.83±0.04
Hajime Saito et al. in [15]	214 single small solitary nodules with diameter <15 mm	The extent of the ratio of ground-glass opacity and circumference difference	Sensitivity is 96.6 %, specificity is 86.1 %, and positive predictive value is 94.1 %
Ayman El-Baz et al. in [16, 17]	327 nodules (153 malignant and 174 benign)	Mesh model of 3D shape	93.6 % correct classification
Ingrid C. Sluimer et al. in [21]	116 patients, 657 regions of interest (ROIs)	Extracting features to describe local image structure by means of a multi-scale filter bank	The Az value is 0.862
Kohei Arai et al. in [23]	14 patients with 5 classes of lung cancer	2D and 3D local binary pattern (LBP) features [23]	The classification accuracy of 2D and 3D LBP are 43 and 78 % respectively

References

1. Lung Cancer. http://www.ncbi.nlm.nih.gov/pubmedhealth/PMH0004529/
2. Swensen SJ, Jett JR, Sloan JA, Midthun DE, Hartman TE, Sykes A-M, Aughenbaugh GL, Zink FE, Hillman SL, Noetzel GR, Marks RS, Clayton AC, Pairolero PC: Screening for lung cancer with low-dose spiral computed tomography. Am J Respir Crit Care Med 165(4): 508–513, 2002
3. MacMahon H, Austin JHM, Gamsu G, Herold CJ, Jett JR, Naidich DP, Patz EF, Swensen SJ: Guidelines for management of small pulmonary nodules detected on ct scans: a statement from the Fleischner society. Radiology 237:395–400, 2005
4. Matsuki Y, Nakamura K, Watanabe H, Aoki T, Nakata H, Katsuragawa S, Doi K: Usefulness of an artificial neural network for differentiating benign from malignant pulmonary nodules on high-resolution CT: evaluation with receiver operating characteristic analysis. Am J Roentgenol 178:657–663, 2002
5. Cardillo G, Regal M, Sera F, Di Martino M, Carbone L, Facciolo F, Martelli M: Videothoracoscopic management of the solitary pulmonary nodule: a single-institution study on 429 cases. Ann Thorac Surg 75:1607–1612, 2003
6. Li F, Aoyama M, Shiraishi J, Abe H, Li Q, Suzuki K, Engelmann R, Sone S, MacMahon H, Doi K: Radiologists' performance for differentiating benign from malignant lung nodules on high-resolution CT using computer estimated likelihood of malignancy. Am J Roentgenol 183:1209–1215, 2004
7. Gould MK, Fletcher J, Iannettoni MD, Lynch WR, Midthun DE, Naidich DP, Ost DE: Evaluation of patients with pulmonary nodules: when is it lung cancer? ACCP Evid Based Clin Pract Guidelines Chest 132:108S–130S, 2007
8. McNitt-Gray MF, Hart EM, Wyckoff N, Wyckoff N, Sayre JW, Goldin JG, Aberle DR: A pattern classification approach to characterizing solitary pulmonary nodules imaged on high resolution CT: preliminary results. Med Phys 26(6):880–888, 1999
9. Li Q, Li F, Shiraishi J, Katsuragawa S, Sone S, Doi K: Investigation of new psychophysical measures for evaluation of similar images on thoracic computed tomography for distinction between benign and malignant nodules. Med Phys 30(10):2584–2593, 2003
10. Zinovev D, Raicu D, Furst J, Armato III, SG: Predicting radiological panel opinions using a panel of machine learning classifiers. Algorithms 2:1473–1502, 2009
11. Yankelevitz DF, Reeves AP, Kostis WJ, et al: Small pulmonary nodules: volumetrically determined growth rates based on CT evaluation. Radiology 217:251–256, 2000
12. Goodman LR, Gulsun M, Washington L, Nagy PG, Piacsek KL: Inherent variability of CT lung nodule measurements in vivo using semiautomated volumetric measurements. Am J Roentgenol 186: 989–994, 2006
13. Iwano S, Nakamura T, Kamioka Y, Ishigaki T: Computer-aided diagnosis: a shape classification of pulmonary nodules imaged by high-resolution CT. Comput Med Imaging Graph 29:565–570, 2005
14. Way TW, Hadjiiski LM, Sahiner B, Chan H-P, Cascade PN, Kazerooni EA, Bogot N, Zhou C: Computer-aided diagnosis of pulmonary nodules on CT scans: segmentation and classification using 3D active contours. Med Phys 33(7):2323–2337, 2006
15. Saito H, Minamiya Y, Kawai H, Nakagawaa T, Ito a M, Hosonoa Y, Motoyamaa S, Hashimotob M, Ishiyamab K, Ogawa J-I: Usefulness of circumference difference for estimating the likelihood of malignancy in small solitary pulmonary nodules on CT. Lung Cancer 58: 348–354, 2007
16. El-Baz A, Gimel'farb GL, Falk R, El-Ghar MA: Appearance Analysis for Diagnosing Malignant Lung Nodules. Proc. of IEEE International Symposium on Biomedical Imaging: From Nano to Macro (ISBI'10), Rotterdam, The Netherlands, April 14–17, 2010, 193–196
17. El-Baz A, Nitzken M, Khalifa F, Elnakib A, Gimel'farb G, Falk R, El-Ghar MA: 3D shape analysis for early diagnosis of malignant lung nodules. Inf Process Med Imaging 22:772–783, 2011
18. El-Baz A, Nitzken M, Vanbogaert E, Gimel'farb GL, Falk R, El-Ghar MA: A Novel Shape-Based Diagnostic Approach for Early Diagnosis of Lung Nodules. Proceedings of the 8th IEEE International Symposium on Biomedical Imaging, 2011, 137–140
19. El-Baz A, Gimel'farb GL, El-Ghar MA, Falk R: Appearance-Based Diagnostic System for Early Assessment of Malignant Lung Nodules. In: Proc. IEEE International Conference on Image Processing (ICIP'12), Orlando, Florida, USA, September 30-October 3, 2012, 1463–1466
20. Vittitoe NF, Baker JA, Floyd CE: Fractal texture analysis in computer-aided diagnosis of solitary pulmonary nodules. Acad Radiol 4:96–101, 1997
21. Sluimer IC, van Waes PF, Viergever MA, van Ginneken B: Computer-aided diagnosis in high resolution CT of the lungs. Med Phys 30(12):3081–3090, 2003
22. SK Vijai Anand: Segmentation and Coupled Textural Feature Classification for Lung Tumor Prediction. IEEE International Conference on Communication Control and Computing Technologies, 2010, 518–524
23. Arai K, Herdiyeni Y, Okumura H: Comparison of 2D and 3D local binary pattern in lung cancer diagnosis. Int J Adv Comput Sci Appl 3(4):89–95, 2012
24. Haralick RM, Shanmugam K, Dinstein I: Textural features for image classification. IEEE Trans Syst Man Cybern SMC-3(6):610–621, 1973
25. Gabor D: Theory of communication. J Inst Electr Eng 93(26):429–457, 1946
26. Wang L, He D: Texture classification using texture spectrum. Pattern Recogn 23:905–910, 1990
27. Samuel G, Armato III, Mclennan G, Bidaut L, McNitt-Gray MF, Meyer CR, Reeves AP, Zhao B, Henschke CI, Hoffman EA, Kazerooni EA, MacMahon H, van Beek EJR, Yankelevitz D, Biancardi AM, Bland PH, Brown MS, Engelmann RM, Laderach GE, Max D, Pais RC, Qing DP-Y, Roberts RY, Smith AR, Starkey A, Batra P, Caligiuri P, Farooqi A, Gladish GW, Jude CM, Munden RF, Petkovska I, Quint LE, Schwartz LH, Sundaram B, Dodd LE, Fenimore C, Gur D, Petrick N, Freymann J, Kirby J, Hughes B, Casteele AV, Gupte S, Sallam M, Heath MD, Kuhn MH, Dharaiya E, Burns R, Fryd DS, Salganicoff M, Anand V, Shreter U, Vastagh S, Croft BY, Clarke LP: The Lung Image Database Consortium (LIDC) and Image Database Resource Initiative (IDRI): a completed reference database of lung nodules on CT scans. Med Phys 38:915–931, 2011
28. Abdi H, Williams LJ: Principal component analysis. Wiley Interdiscip Rev Comput Stat 2:433–459, 2010
29. Kamarainen J-K, Kyrki V, Kälviäinen H: Invariance properties of gabor filter-based features—overview and applications. IEEE Trans Image Process 15(5):1088–1099, 2006
30. Kruizinga P, Petkov N, Grigorescu SE: Comparison of Texture Features Based on Gabor Filters. Proceedings of the 10th International Conference on Image Analysis and Processing, Venice, Italy, September 27–29, 1999, 142–147
31. Petkov N, Kruizinga P: Computational models of visual neurons specialised in the detection of periodic and aperiodic oriented visual stimuli: bar and grating cells. Biol Cybern 76:83–96, 1997
32. Jones JP, Palmer LA: An evaluation of the two-dimensional gabor filter model of simple receptive fields in cat striate cortex. J Neurophysiol 58:1233–1258, 1987
33. Ojala T, Pietikäinen M, Harwood D: A comparative study of texture measures with classification based on feature distributions. Pattern Recogn 29(1):51–59, 1996

34. Ahonen T, Hadid A, Pietikäinen M: Face description with local binary patterns: application to face recognition. IEEE Trans Pattern Anal Mach Intell 28(12):2037–2041, 2006
35. Heikkilä M, Pietikäinen M, Schmid C: Description of interest regions with local binary patterns. Pattern Recogn 42(3):425–436, 2009
36. Philips C, Li D, Furst J, Raicu D: An Analysis of Co-Occurrence and Gabor Texture Classification in 2D and 3D. CARS 2008 Proceedings. Barcelona, Spain
37. Zhang G, Wang T, Lu H, Zhang J, Liu X, Liang Z: CAD Based on 3D Texture Analysis for Virtual Colonoscopy. The 22nd International Congress and Exhibition, CARS 2008 Computer Assisted Radiology and Surgery, June 25–28, 2008, Barcelona, Spain: 17
38. Han F, Wang H, Song B, Zhang G, Lu H, et al: A New 3D Texture Feature Based Computer-Aided Diagnosis Approach to Differentiate Pulmonary Nodules. Proc. SPIE 8670, Medical Imaging 2013: Computer-Aided Diagnosis, 86702Z, February 28, 2013
39. Philips C, Li D, Raicu D, Furst J: Directional Invariance of Co-Occurrence Matrices within the Liver. International Conference on Biocomputation, Bioinformatics, and Biomedical Technologies, 2008, 29–34
40. Suykens J, Vandewalle J: Least squares support vector machine classifiers. Neural Process Lett 9(3):293–300, 1999
41. Fritsch FN, Carlson RE: Monotone piecewise cubic interpolation. Soc Ind Appl Math 17(2):238–246, 1980
42. Han H, Li L, Han F, Zhang H, Moore W, Liang Z: Vector Quantization-Based Automatic Detection of Pulmonary Nodules in Thoracic CT Images. In Proc. of IEEE Nuclear Science Symposium and Medical Imaging Conference, Seoul, Korea, October 27 - November 2, 2013
43. Fan L, Song B, Gu X, Liang Z: Improved Computer-Aided Colonic Polyp Detection Using a Modified SVM Classifier with Adaptive Kernel. Conf Record IEEE NSS-MIC, in CD-ROM, 2012
44. Zhang G, Liang Z, Song B, Zhu H, Lu H: A Virtual Pathology Model for Differentiation of Colonic Polyp Types for CT Colonography. The 98th Annual Meeting of the Radiological Society of North America (RSNA), 2012, 414
45. Song B, Zhang G, Zhu H, Zhu W, Lu H, Liang Z: A Feasibility Study of High Order Volumetric Texture Features for Computer Aided Diagnosis of Polyps via CT Colonography. Conf Record IEEE NSS-MIC, in CD-ROM, 2012
46. Wang J, Li T, Hongbing L, Liang Z: Penalized weighted least-squares approach to sinogram noise reduction and image reconstruction for low-dose x-ray CT. IEEE Trans Med Imaging 25(10):1272–1283, 2006
47. Liu Y, Ma J, Fan Y, Liang Z: Adaptive-weighted total variation minimization for low-dose X-ray computed tomography image reconstruction. Phys Med Biol 57:7923–7956, 2012